JOURNAL OF AIRCRAFT
Vol. 44, No. 5, September–October 2007

Aerodynamic Characteristics of a Free-Wing Tilt-Body Unmanned Aerial Vehicle

Kapseong Ro* and Kaushik Raghu†
Western Michigan University, Kalamazoo, Michigan 49008
and
Jewel B. Barlow‡
University of Maryland, College Park, Maryland 20742

DOI: 10.2514/1.27989

The free-wing tilt-body concept demonstrated excellent flight performance characteristics, including extremely short takeoff and landing and excellent gust load alleviation, through a prototype unmanned aerial vehicle flight test. Though some wind-tunnel tests were carried out to investigate the aerodynamic characteristics, there is still a need to further understand the intrinsic nature of its complex aerodynamic properties, which leads to possible design refinements and vehicle-performance-parameter optimization studies. In this paper, the aerodynamic characteristics of a generic free-wing tilt-body configuration were studied using a numerical aerodynamic analysis based on the panel method. The computed aerodynamic coefficients were compared with the previously reported wind-tunnel test results for verification and validation. The numerical aerodynamic analysis employed showed comparable results when compared with the experimental results, despite some discrepancies that are believed to be mostly due to known differences in the model geometries and the limitations of the panel method.

Nomenclature

b	=	wing span
Re	=	Reynolds number
α_F	=	body-reference-line geometric angle of attack
α_W	=	free-wing geometric angle of attack
γ	=	flight-path angle
δ_B	=	boom angle
θ_W	=	free-wing pitch angle relative to the body-reference line
θ_F	=	body-reference-line pitch angle

I. Introduction

UNMANNED aerial vehicles (UAVs) are now considered to be an integral part of modern military operations, and their roles continue to expand in military missions and in various civil applications. Among the variety of UAV types and applications, an UAV platform with vertical/short takeoff and landing (VSTOL) capability is in great demand. One promising platform is the free-wing tilt-body aircraft, such as that shown in Fig. 1, which demonstrated extremely short takeoff and landing (ESTOL) capability through prototype flight tests. The vehicle does not employ complicated rotating mechanisms such as rotor-based vertical takeoff and landing (VTOL) aircraft; rather, it has an articulated wing–body–tail configuration in which the the wing, body, and empennage are in a longitudinally articulated connection, allowing the main wing to freely rotate relative to the body as it adjusts to the freestream velocity. The empennage is in the form of a long twin boom connected to the end of the body. The boom changes its incidence angle relative to the body in response to external torque commands through a control horn. Displacement of the tail relative to the body produces a pitching moment on the entire aircraft as the aerodynamic force on the tail tends to align it with the direction of flight. With the propulsion system mounted on the body and thereby providing thrust force along the body centerline, the configuration has a novel thrust-vectoring capability, in addition to excellent gust response properties provided by the free wing.

The concept of an articulated wing and fuselage was first revealed in a patent in 1945 by Zuck [1], who called it a rotatable wing or free wing, and this concept was applied to a flying boat built by Spratt [2] in 1952. Some experimental work and limited analytical studies were carried out by NASA researchers in the 1970s [3–5]. In 1986, the Freewing Aircraft Corporation built and patented [6] an ultralight aircraft based on the free-wing concept for improved stall resistance and reduced gust sensitivity and later introduced the tilt-body concept in conjunction with a free wing to build the Freewing Tiltbody™ unmanned aerial vehicle (UAV), called Scorpion (Fig. 1). The tilt-body feature was introduced in response to a requirement for reduced takeoff and landing footprints. The Scorpion has a unique body configuration in the form of a blended wing–body shape generating a significant portion of the total aerodynamic loads. In addition, the propeller slipstream effect on the body and free wing is quite significant. The boom-angle change during flight substantially alters the aerodynamic loads and inertial properties of the entire vehicle, in contrast to a typical moment-trimming surface in a conventional airplane. Consequently, the resultant aerodynamic-load production is far more complex than that of a fixed-wing aircraft, and thus conventional fixed-wing aerodynamic analysis is not adequate. The process of selecting design parameters and carrying out the relevant analyses to support the choices made is equivalent to doing so for entire families of fixed-wing vehicles. On the other hand, to be considered as a competitive UAV platform, the vehicle must achieve a high level of autonomy through comprehensive model-based design and analysis and hardware-in-the-loop simulation (HILS) tests. Such studies require in-depth understanding of flight dynamic characteristics, which are heavily dependent upon reliable and comprehensive configuration aerodynamic data.

The objective of this paper is to investigate the aerodynamic characteristics of a free-wing tilt-body configuration similar to the Scorpion UAV through numerical aerodynamic analysis (panel methods). Numerical aerodynamic analysis is a very effective tool to

Received 24 September 2006; accepted for publication 28 November 2006.

*Assistant Professor, Department of Mechanical and Aeronautical Engineering, College of Engineering and Applied Science. Member AIAA.
†Research Assistant, Department of Mechanical and Aeronautical Engineering, College of Engineering and Applied Science. Student Member AIAA.
‡Director, Glenn. L Martin Wind Tunnel, Department of Aerospace Engineering, College of Engineering. Associate Fellow AIAA.

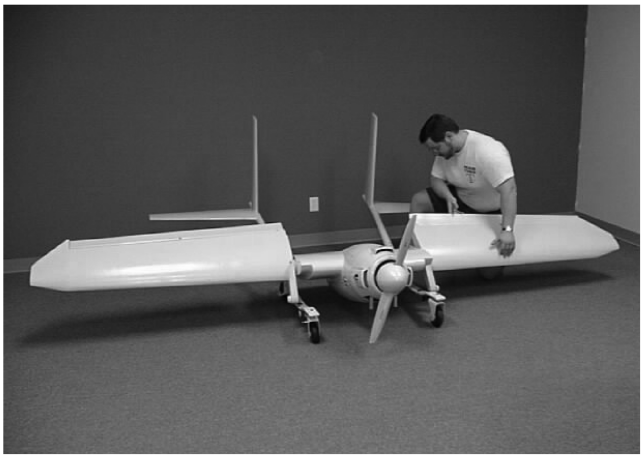

Fig. 1 Scorpion unmanned aerial vehicle (wind-tunnel model).

assist in understanding the intrinsic nature of flowfield characteristics through graphical visualization of flowfield properties such as pressure, velocity, streamlines, etc., at any particular region of interest. Furthermore, it can be used for iterative design studies to optimize vehicle performance parameters. These features are particularly useful to study the complex nature of the aerodynamics of free-wing tilt-body aircraft and to address possible design refinements. The outcome of this research, combined with the experimental results from the Glenn L. Martin Wind Tunnel (GLMWT) at the University of Maryland [7], provides sufficient information to study the vehicle flight characteristics, which can lead to design refinement and allow parameter optimization for selected performance metrics.

II. Vehicle Description

The vehicle geometry is summarized in Table 1. It is a generic free-wing tilt-body configuration similar to the Scorpion UAV, which in turn is comparable to the 60%-scale model used for the wind-tunnel experiment at the GLMWT. It is important to carefully define and understand the angles that characterize the vehicle attitude and aerodynamic loads, due to the articulated wing–body–tail configuration. Figure 2 shows the necessary angles to characterize the longitudinal motion of the vehicle. From this figure, it can be observed that the free-wing geometric angle of attack α_W is the sum of the free-wing pitch angle θ_W (the angle between the body-reference line and the free-wing chord line) and the body angle of attack α_F (i.e., $\alpha_W = \theta_W + \alpha_F$). The free-wing pivot point relative to the body is located ahead of the free-wing aerodynamic center to provide inherent aerodynamic stability for the wing. A force is transmitted through the wing pivot to the body, but no moment component in the direction of the wing pivot axis is transmitted to the body. The direction of the wing pivot axis in this study is in the direction of the pitching moment. The thrust direction is assumed to be fixed along the body-reference line and the boom angle is defined with respect to it. The boom deflection by a control horn affects aerodynamic force on the horizontal tail, which in turn produces pitching moment. This pitching moment sets the centerbody to a certain angle of attack, thus providing a thrust-vectoring capability. When the body angle of attack changes, the free-wing pitch angle θ_W also changes as necessary to achieve zero pitching moment about the wing pivot axis in the new flight condition.

Longitudinal control is achieved by elevon, tail boom, and throttle setting. The elevon is a full-span trailing-edge device on the free wing. The free-wing angle of attack, and thus its lifting power, is directly controlled by the symmetric deflection of the elevon, whereas the zero pitching moment about the wing pivot axis is transmitted to the main body. Therefore, the symmetric deflection of the elevon is acting as a direct lift control (DLC) device rather than a pitch control device. The primary pitch control is achieved through the tail-boom angle, which changes the body angle of attack. The

Table 1 Vehicle geometry summary

Items	Configuration
Aircraft	
Wing span, ft	7.7
Reference area, ft^2	12.51
Free wing	
Area, ft^2	6.775
Taper ratio	0.804
Aspect ratio	4.25
Airfoil	Proprietary
Pivot location from the leading edge	20% chord
Center body	
Span, ft	2.333
Area, ft^2	5.735
Fuselage length, ft	3.5
Horizontal tail	
Area, ft^2	2.718
Root chord, ft	1.13
Taper ratio	0.485
Airfoil	Flat plate
Vertical tail	
Root chord, ft	0.79
Taper ratio	0.527
Span, ft	2.076
Area, ft^2	2.41
Airfoil	Flat plate

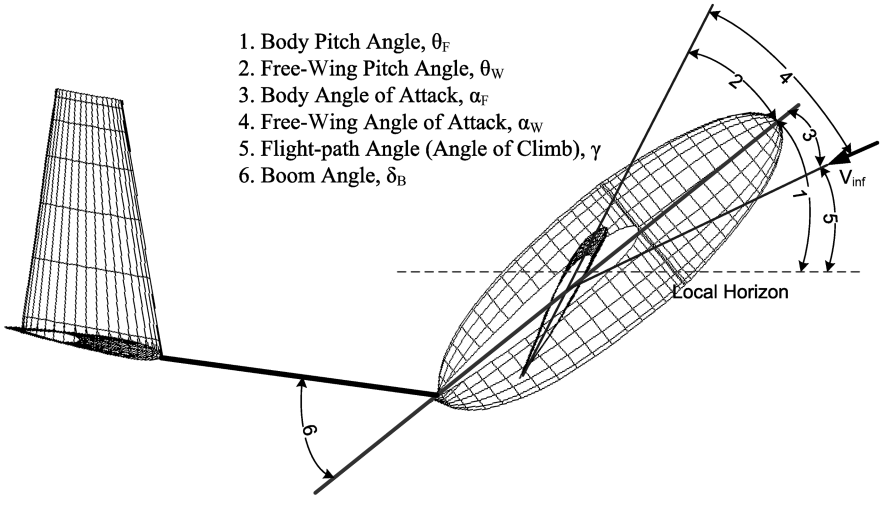

Fig. 2 Angle definition for the free-wing tilt-body.

tilting of the body changes the direction of the thrust vector and thus substantially contributes to the total vehicle lift when the engine is operating at moderate to high power levels. This allows the vehicle to maintain much lower speeds than a fixed wing and to descend at steep slopes at a slow speed. The lateral control is achieved by differential deflection of the full-span control surfaces on the wings. The prototype vehicle does not have a rudder, but it may be advantageous to have rudder control for the highest boom-angle configurations. The lateral dynamics are largely similar to fixed-wing vehicles in the low boom-angle configuration, but should differ significantly for high boom angles.

III. Configuration Aerodynamic Analysis

The free-wing tilt-body has complex aerodynamic characteristics, due to inherent and potentially large vehicle-configuration changes during flight. Empirical and analytical prediction methods widely used for fixed-wing aircraft aerodynamics become problematic for some of the flight conditions, and thus extensive wind-tunnel tests and/or numerical simulation studies are needed. The numerical simulation technique used in this paper is a panel method that incorporates the usual assumptions of ideal inviscid flow with Kutta conditions applied as guided by historical experimental results. A software tool based on the panel methods called CMARC, developed by AeroLogic, Inc., is used to solve for flow and pressure around the free-wing tilt-body aircraft. The software is based upon the well-known panel method, Ames Research Center, version 12 (PMARC 12). It retains important advanced features of PMARC 12 such as a time-stepping wake, a Trefftz plane calculation of induced drag, and two-dimensional integral boundary-layer methods, etc. Along with CMARC, the software package provides a graphical lofting tool (LOFTSMAN) to create a numerical mesh model and a postprocessing tool (POSTMARC) for the resultant load calculation, various flowfield analyses, and total load calculations.

The GLMWT test results indicate that the aerodynamic loads of the Scorpion are seldom close to a simple addition of those of the individual components. This is due to strong aerodynamic interaction among the components, which also varies strongly as the configuration changes for varying flight conditions. In addition, the effect of the propeller slipstream adds even more complexity in the entire vehicle aerodynamic field. The present studies are aimed at investigating the flowfield properties of each component and their interactions at different flight configurations through the use of the panel method. The numerical solutions enable the graphical visualization of the flowfield properties, from which the effect of important design parameters can be observed, along with their impact on flight performance characteristics.

For verification and validation purposes, the aerodynamic loads predicted by the numerical aerodynamic analysis were compared with the experimental results of the GLMWT. The numerical aerodynamic analysis was performed at a chord Reynolds number Re of 1.02×10^5 to be comparable with the GLMWT experimental results. It is to be noted that there are some known differences in the geometries of the wind-tunnel test model shown in Fig. 1 and the grid model used for numerical analysis shown in Fig. 3, because some elements of the actual geometry must be approximated or even neglected to achieve solutions with the resources available for this study. The lifting portion of the body in the wind-tunnel model is positioned like a high-wing configuration and is not exactly aligned with the centerline of the nonlifting portion, whereas it is modeled as a symmetric body in the x–y plane and in the x–z plane with the NACA0012 airfoil section. In addition, the details of the free-wing section geometry are not exactly known for the wind-tunnel test model, whereas the NACA 2412 section was implemented in the numerical model. The booms were not included in the numerical model, because their contributions to the total aerodynamic loads were considered insignificant while causing substantial numerical difficulties, often causing erroneous solutions. Nevertheless, the results obtained from the numerical aerodynamic analysis reflect the important properties of the vehicle configuration, because they generally agree with the GLMWT experimental data.

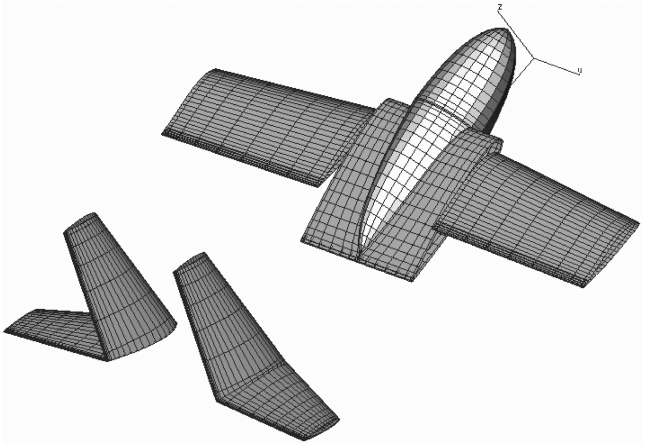

Fig. 3 Grid model for numerical analysis.

A. Flow Around the Body Only

Because the body of the Scorpion UAV produces substantial aerodynamic loads, it produces significant induced flow on the free wing and the empennage. For this reason, the flowfield around the body isolated from the free wing was modeled. In addition, the body and free-wing assembly and their influences on the tail empennage were investigated.

Figure 4 depicts the on-body streamlines and flowfield characteristics in terms of the coefficient of pressure contour plots for the body-only configuration at several body angles of attack. At lower angles of attack ($\alpha_F \leq 10$ deg), the on-body streamlines on the top and bottom surfaces (Figs. 4a and 4b) are relatively evenly spaced and straight from the leading edge to the trailing edge on the body-wing portion. It is also interesting to observe the pressure change across the trailing-edge line: the pressure reaches a maximum at the tip of the fuselage due to its streamline curvature. The region of low pressure is well defined on the upper region of the fuselage and body wing (lifting portion of the body) in both the chordwise, as shown in Fig. 4c, and spanwise directions, as shown in Fig. 4d. All of these indicate that the flow should be well attached, and thus it is reasonable to assume that predicted aerodynamic loads would be comparable with empirical results. The contour plot taken at the trailing-edge plane in Fig. 4e also supports the preceding observations, because the strength of the tip vortices is not significant compared with the high-pressure buildup along the trailing-edge line. This implies that the spanwise crossflow is relatively insignificant.

As the body angle of attack increases, the streamlines on the top surface in Fig. 4a move further inward in the spanwise direction as they travel downstream, whereas the streamlines on the bottom surface move toward the wingtip, as shown in Fig. 4b, indicating the dominant lift-induced flow effect. Observing Fig. 4b at $\alpha_F = 30$ and 40 deg, the region of high pressure on the body wing is rapidly building up from the center, due to the fuselage curvature. This indicates that the presence of the fuselage induces spanwise flow toward the wingtips, resulting in rapid buildup of the high-pressure region, thus the lifting portion of the body becomes more efficient in lift production, which can be well observed in Fig. 4d at $\alpha_F = 30$ deg. On the other hand, the region of low pressure on the upper portion of the body is beginning to split in the spanwise direction at $\alpha_F = 30$ deg, as shown in Fig. 4d, implying that the fuselage gets less effective in lift production. Flow separation is evident over the forebody portion at $\alpha_F \geq 30$ deg, due to rapid buildup of the high-pressure region at the rear portion of the body, resulting in a large velocity gradient. The nature of flow separation for this configuration is uncertain in detail, and thus is not incorporated into the numerical solution. However, substantial lift would be still generated by the body wing, as can be seen in Fig. 4d. At $\alpha_F = 40$ deg, there is a dominant region of high pressure on the bottom and aft portions of the body (Figs. 4c and 4d), and signs of likely flow separation are evident on the body-wing area. Thus, it can be concluded that the body would stall somewhere in the range of 30 deg $\leq \alpha_F \leq$ 40 deg.

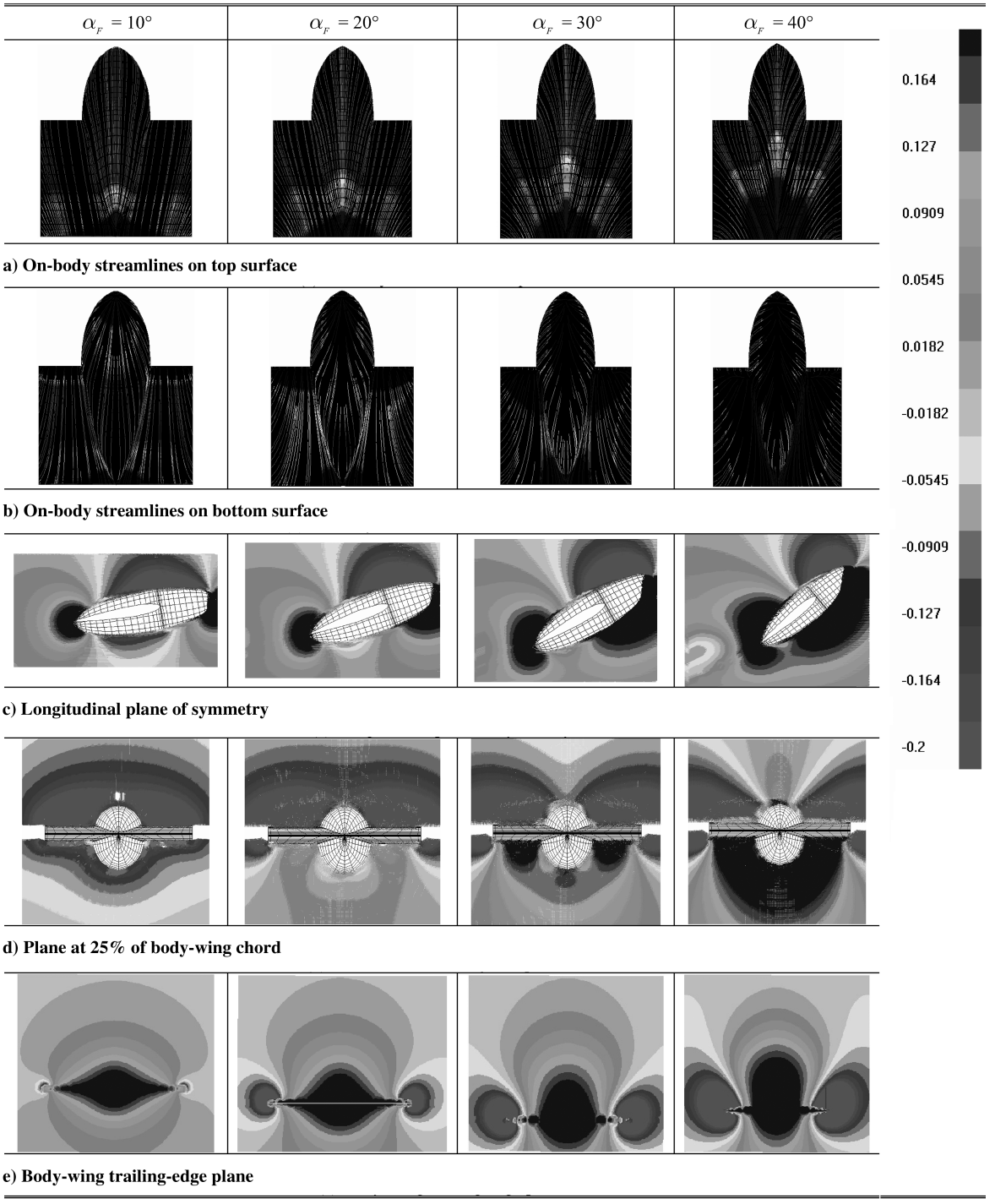

Fig. 4 Flowfield (coefficient of pressure) analysis for the body.

Strengthened tip vortices are evident as the angle of attack increases in Fig. 4e, and they strongly interact with the high-pressure region on the aft fuselage. A large pressure gradient along the trailing-edge line is apparent, which influences the stall characteristics of the body.

B. Flow Around the Body and Free-Wing Assembly

As mentioned earlier, the free wing adjusts its angle of attack so that there is zero moment about the free-wing pivot axis as the body changes its angle of attack in response to the boom deflection. This is because it is free to rotate (i.e., zero pitching moment) about its pivot axis, which is at 20% of its own chord. In other words, there is a functional relationship, $\alpha_W = f(\alpha_F)$, as shown in the GLMWT test results and given here in Fig. 5. This result indicates that the free wing retains a negative angle of attack as the body angle of attack

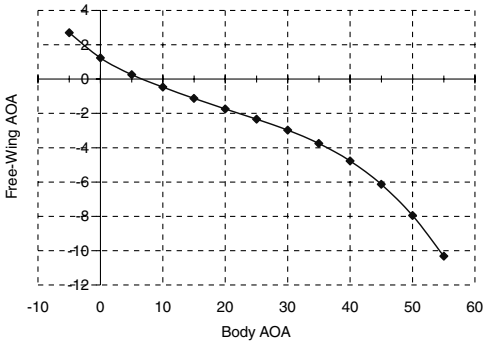

Fig. 5 Body angle of attack vs free-wing angle of attack.

increases. This implies the presence of upwash on the free wing due to the body tip vortices. This upwash is also implied from the on-body streamline results in Fig. 6. Finding such a relationship through numerical aerodynamic analysis would be difficult, because it requires either dynamic modeling that requires inertial and damping properties of the free wing or at least iterative solutions with some algorithm to converge to a condition representing the free-to-pitch condition. We have not undertaken that problem in this study. Instead, the free-wing angle of attack was set to the experimentally observed values corresponding to the angle of attack of the body. The procedure we followed allows investigation of the aerodynamic interaction effects between the body and free wing, so as to logically compare numerical results with the GLMWT empirical results that are discussed in Sec. IV.

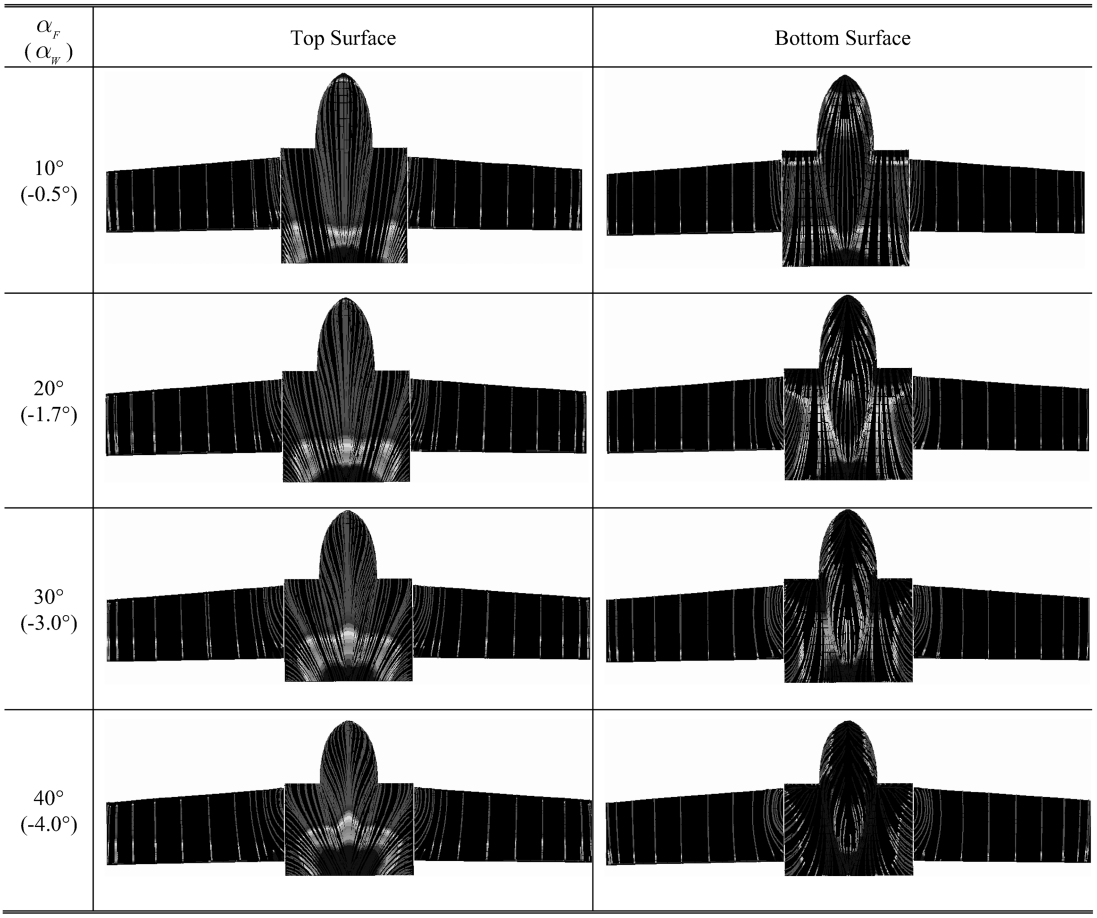

Fig. 6 On-body streamlines on the body and free-wing assembly with free-wing pitch set at the experimentally observed value.

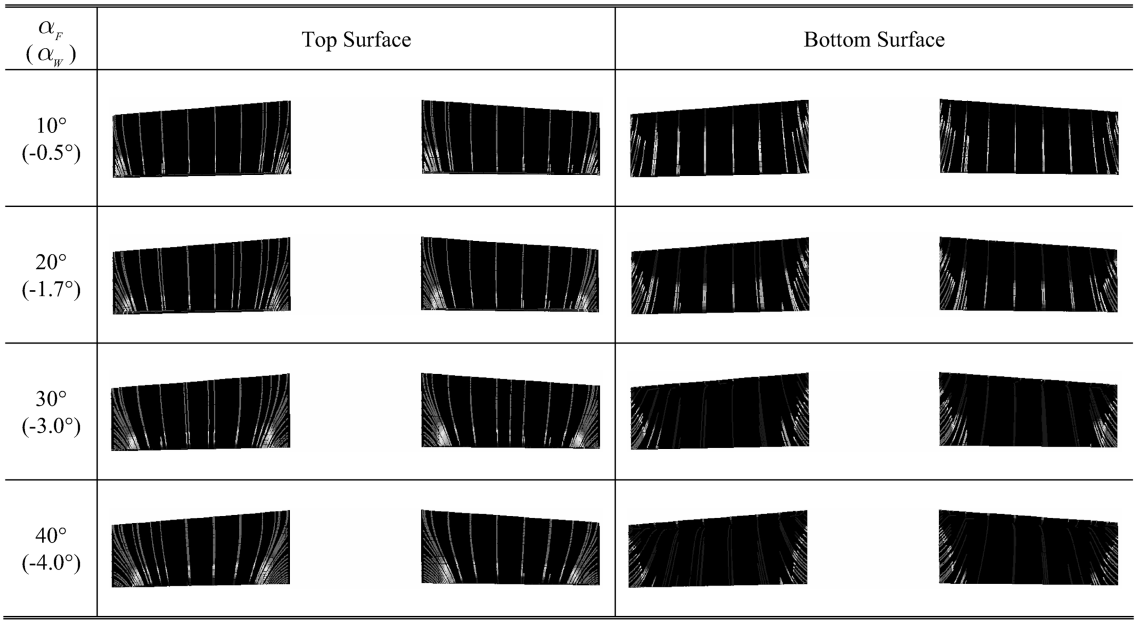

Fig. 7 On-body streamlines on the free wing only with its angle of attack set at the experimentally observed value.

Figure 6 gives the on-body streamline patterns for the body and free-wing assembly. Observing the body and free-wing junction and comparing the on-body streamline patterns for the free-wing-only case with its angle of attack set at the experimentally observed values corresponding to the angle of attack of the body shown in Fig. 7, it is apparent that the body significantly alters the flow pattern on the free wing and its influence gets larger and larger as the body angle of attack increases. This is not a surprise. It indicates that the spanwise crossflow or lift-induced flow from the body alters the pressure field of the free wing, particularly at the junction, resulting in the negative angle of attack observed in the GLMWT test results shown in Fig. 5.

The aerodynamic interaction effect is further illuminated by examining the chordwise pressure-field characteristics on the plane defined at the $0.15(b/2)$ (on the body-wing portion) and the $0.30(b/2)$ (on the free-wing portion) for the body only and the body and free-wing assembly, as shown in Fig. 8. Note that the free-wing angle of attack is set at 0 deg instead of at the experimentally observed value. This is to clearly delineate the influence of the body on the free wing that results in the negative free-wing angle of attack. Looking at Figs. 8a and 8b, the influences of the free wing on the body are not so apparent from these figures. On the other hand, the effect of the body on the free wing is quite distinct in Figs. 8c and 8d. Basically, the inboard portion of the free wing is located in the region of strong lift-induced flow from the low-aspect-ratio lifting body, and its influence gets stronger as the body angle of attack increases, as discussed earlier. Furthermore, from Fig. 8d, it can be observed that

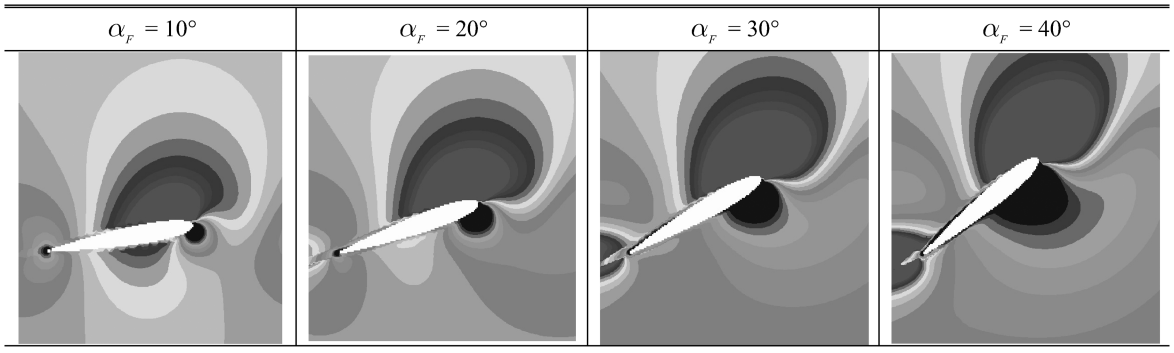

a) Plane at 0.15*b* for the body only

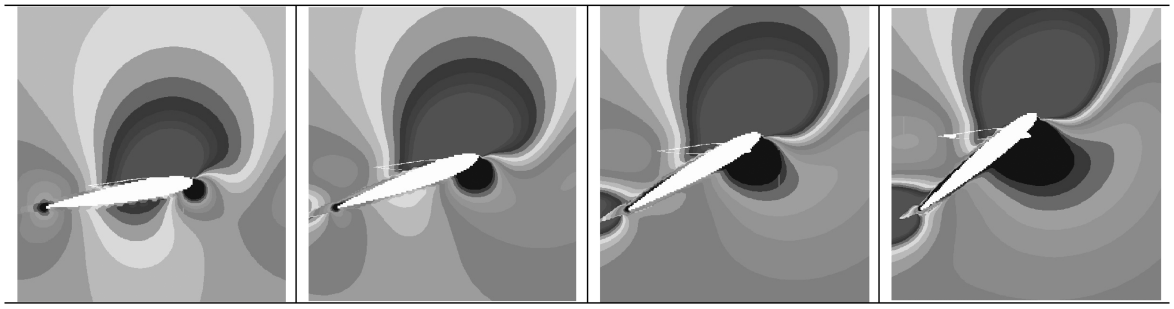

b) Plane at 0.15*b* for the body and free-wing assembly

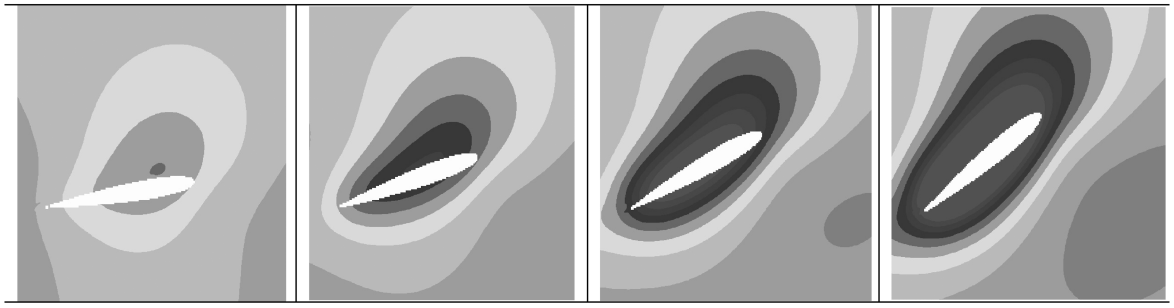

c) Plane at 0.3*b* for the body only

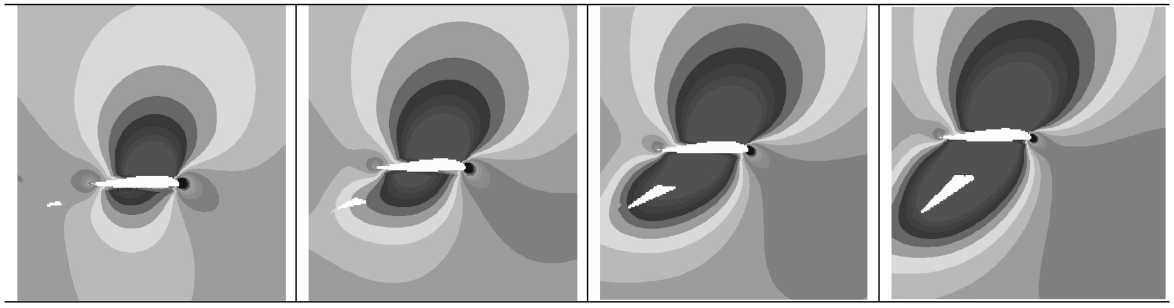

d) Plane at 0.3*b* for the body and free-wing assembly

Fig. 8 Flowfield analysis (pressure coefficient) for the body and free-wing assembly with $\alpha_w = 0$ deg.

the net pressure imbalance between the top and the bottom surfaces appears to lead to a negative pitching moment, thus supporting the negative angle of attack reported in the GLMWT empirical result shown in Fig. 5.

C. Flow Around the Entire Vehicle

In combination with the free wing, the vehicle has a unique tail-boom configuration that gives a means of thrust vectoring. Figure 9 shows the side views for three different boom angles at different body angles of attack, with the free-wing angles of attack set at the experimentally obtained value. Because the body is basically a low-aspect-ratio lifting surface, its tip vortex as it moves downstream has significant effect on the tail. This can be understood by modeling the vortex-induced flow using the time-stepping wake option in CMARC. This allows the wake shape to be modified by the computed flowfield and pressure distribution [8]. Figure 10 illustrates how the stream passes over the body and free-wing assembly and propagates past the tail region during the time-stepping wake computation. It is interesting to observe that the twin tail is designed in such a way that the cores of the body vortices remain between the vertical-tail surfaces, thus preventing the flow over the horizontal-tail surfaces from being obstructed directly by the strong core of the body vortices. Depending upon the boom angle, the horizontal- and vertical-tail efficiencies may change as they interact with the strong body vortices.

The paths of the cores of the body vortices can be seen on Fig. 10 to be nearly parallel with the tail booms for the 20-deg case and only slightly less inclined than the tail booms for the 30- and 40-deg cases. The close proximity of the cores to the vertical tails will be expected to have a strong influence on the lateral stability properties. As mentioned already, the vertical tails provide some shielding of the horizontal surfaces from the influence of the body vortices. As the boom angle is increased to 30 deg and higher, it is seen that the body vortex cores pass below the empennage assembly and will have a corresponding reduction in interaction.

The wake of the free wing may influence the empennage in a fashion similar to that for a conventional fixed wing with aft empennage. The free wing has a relatively large aspect ratio compared with the body, and so its lift-induced flow effects are not as strong as those of the body.

IV. Comparison with GLMWT Experimental Results

To verify the integrity of the panel model and numerically computed values, the convergence of the potential flow solution was checked for each case by observing the values of aerodynamic coefficients during the wake iterations [9]. For those configurations representing the body and the body and free-wing assembly, 20 time-stepping wake iterations were performed and the solution convergence was checked. Figure 11 shows the changes of lift and drag coefficients as functions of the number of iterations for the body and free-wing assembly at $\alpha_F = 10$ deg. Because the values of both coefficients do not change too much after the sixth wake iteration, the numerical solution obtained is considered to be correct. For the entire vehicle, an appropriate number of wake iterations was maintained (mostly 8 to 10 iterations) for each geometric configuration to ensure that the body and free-wing wake stops before it propagates to the empennage panel boundary.

One should not expect precise one-to-one matches of the numerically obtained aerodynamic coefficients to those values experimentally obtained by the GLMWT, because there are some known differences in the geometries and inviscid-flow assumptions of the panel method. Nevertheless, the numerically computed results do exhibit comparable trends in aerodynamic characteristics when compared with the GLMWT experimental results, which will be described shortly. The comparison of the numerical and experimental results supports the validity of the important trends sufficiently to justify use of the panel method as a tool for carrying out design studies of this class of vehicle that undergoes large geometric variations.

A. Body Only

Figure 12 shows the aerodynamic coefficients as functions of the body angle of attack obtained from the numerical aerodynamic analysis, compared with those the GLMWT experimental results for the body only.

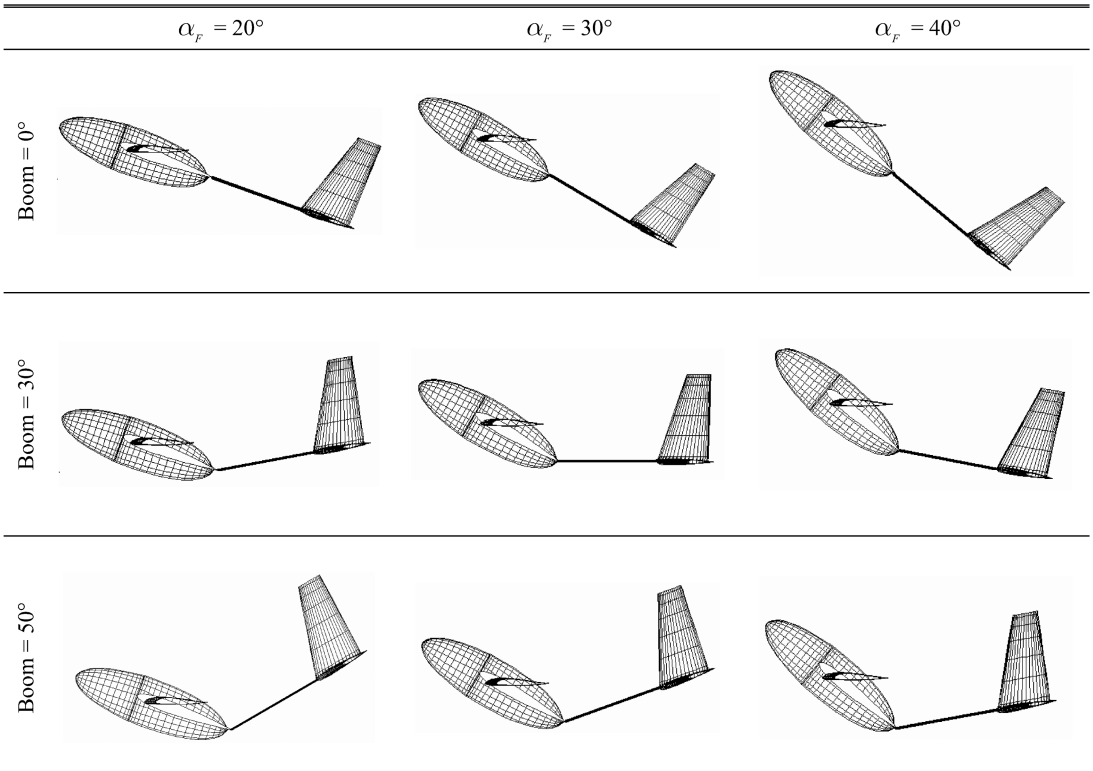

Fig. 9 Body angle vs boom angle.

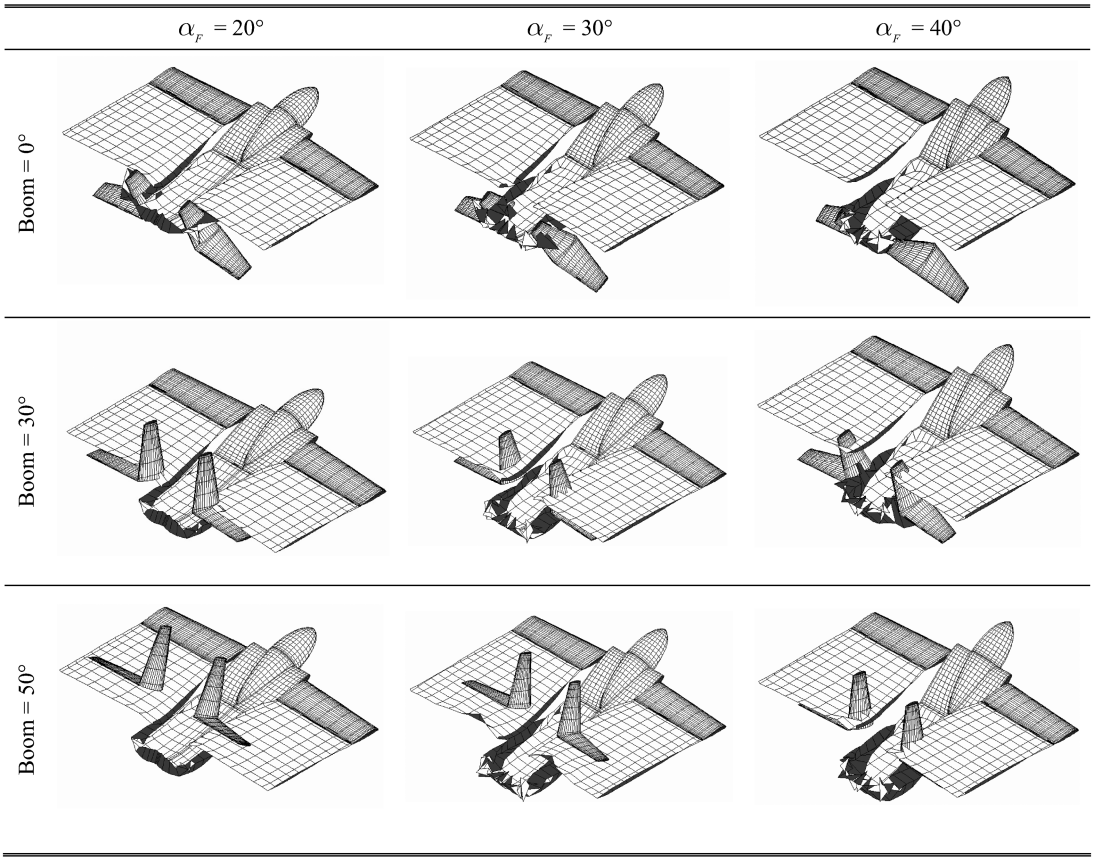

Fig. 10 Induced flow propagation to the tail region.

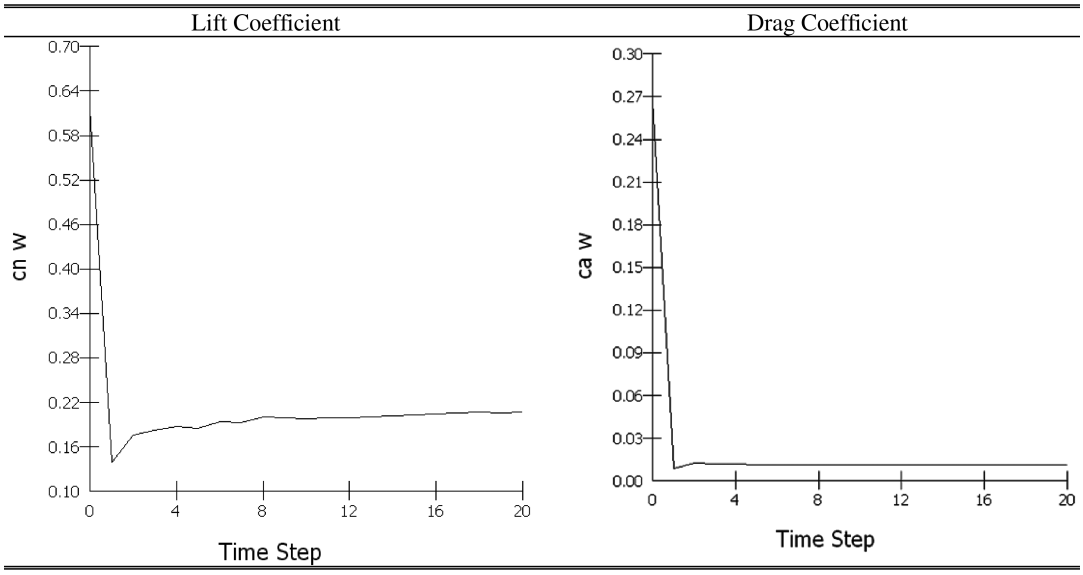

Fig. 11 Changes of aerodynamic coefficients with the number iteration.

For a body angle of attack below 30 deg, the panel-method results for the lift coefficient are lower than the measured values by about 0.05. This difference in lift coefficients between the experimental and numerical values at lower angles of attack ($\alpha_F \leq 30$ deg) may be due to the built-in camber effect in the wind-tunnel model, whereas the numerical mesh is modeled as a symmetrical body. The geometric differences are likely more extensive than just a camber in the wind-tunnel model. The body wing of the wind-tunnel test model is not at the center of the fuselage, and the body-wing zero-lift line is not exactly aligned with the centerline of the fuselage. An angular offset of the fuselage and the body-wing zero-lift line could lead to a shift in the lift curve similar to the difference exhibited here, which will be discussed in the paragraphs on moment coefficient. The high-wing configuration of the body wing may not substantially influence the longitudinal properties, but it would have an impact on the lateral properties. On the other hand, a free-wing camber difference would be expected to have a significant effect on the longitudinal properties. The wind-tunnel data show stall effects beginning around 30 deg. The numerical result does not reflect the stall characteristic, because the necessary boundary-layer information and flow-separation characteristics of this type of body are not well known and thus are not incorporated in the numerical analysis.

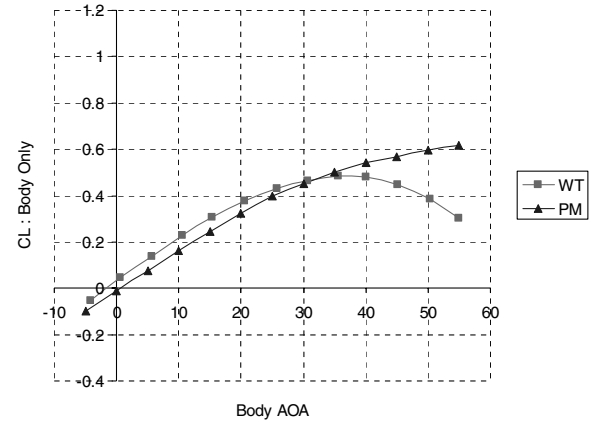

a) Lift coefficient

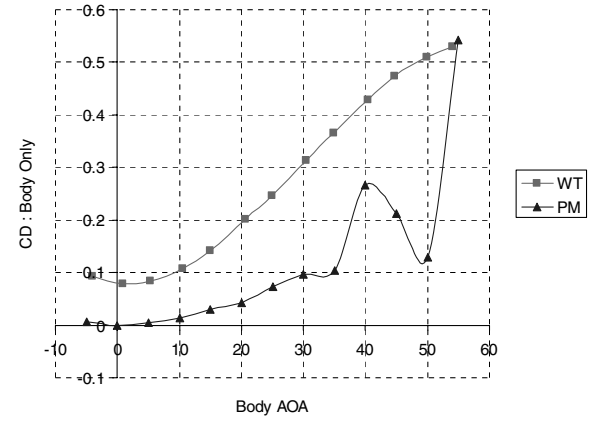

b) Drag coefficient

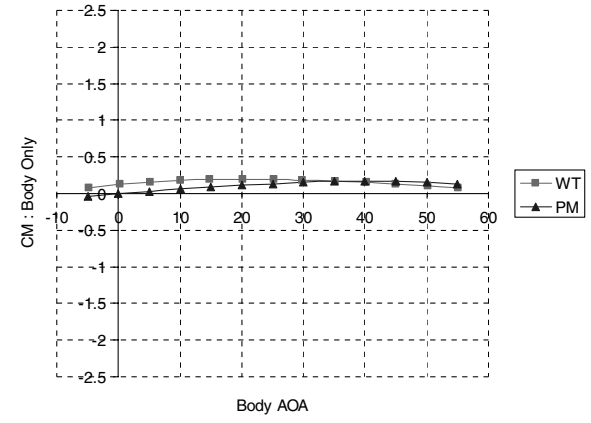

c) Moment coefficient about the pivot axis

Fig. 12 Body aerodynamic-coefficients comparison.

The panel-method results for the drag coefficient are uniformly lower than the experimental results. This is expected because the panel-method drag calculation is primarily induced drag unless one has incorporated the boundary-layer capabilities in the panel-method calculations and modeled the separation locations at other than the trailing edges. The computed drag coefficient in this case only represents the induced drag based on the Trefftz plane analysis. The radical behavior of the drag coefficient for $\alpha_F \geq 35$ deg is not considered realistic, but is shown to indicate difficulties with convergence of the potential flow solution for $\alpha_F \geq 35$ deg. This difficulty is less severe when the wing and tail are added.

The panel-method results for the moment coefficient show a trend similar to that of the experiment. There is a difference, but it

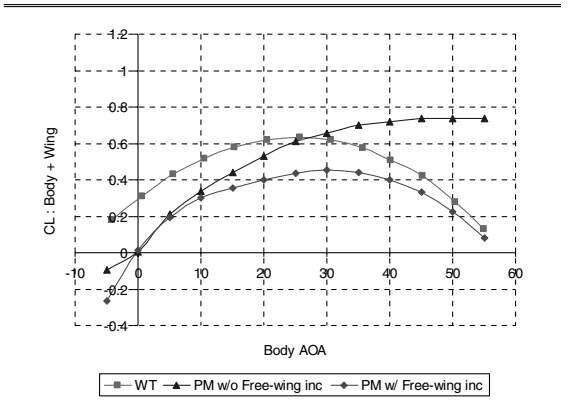

a) Lift coefficient

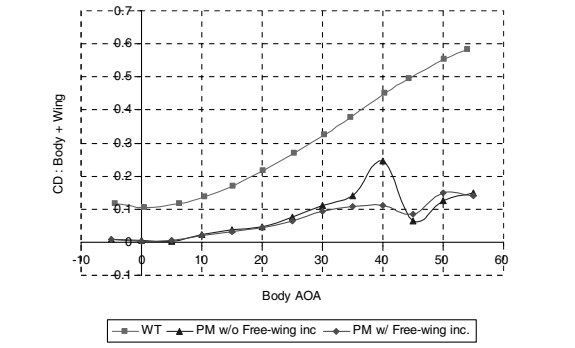

b) Drag coefficient

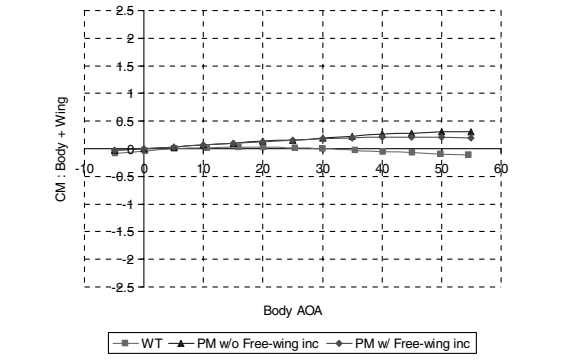

c) Moment coefficient about the pivot axis

Fig. 13 Body and free-wing assembly aerodynamic-coefficients comparison.

is within a range consistent with known geometric differences. Both results are quite small relative to the moment coefficients produced by the complete aircraft configuration, as will be seen in the following.

B. Body and Free Wing

Figure 13 shows the lift, drag, and pitching-moment coefficients for the body and free wing, as obtained from the panel method and from the wind-tunnel experiment. Two curves for the panel method are shown on each plot. One curve corresponds to the free-wing angle of attack being maintained at zero, and the second curve corresponds to the free-wing angle of attack being set as a function of the body angle of attack, as observed in the wind-tunnel experiment shown in Fig. 5. It is the latter that would be expected to more closely correspond to the experimental results.

The lift coefficient from the panel method is approximately 0.2 less than the experimental result for angles of attack less than 30 deg. This could be explained by a difference in camber, recalling that the

panel-method geometry models a symmetric body. The GLMWT experimental results indicate that the body and free-wing assembly stalls at $\alpha_F \cong 25$ deg, which is smaller than the body-only case, which is at $\alpha_F \cong 35$ deg. Observing Fig. 13a, the lift coefficient from the numerical analysis with the zero free-wing angle of attack exhibits no stall phenomenon, as in the body-only case, but those lift coefficients incorporating the experimental free-wing angle of attack show a stall-like behavior, as in the GLMWT test results. The maximum lift coefficient of the body and free-wing assembly occurs at $\alpha_F \cong 25$ deg in the GLMWT test results, whereas the numerical aerodynamic analysis predicts the maximum lift coefficient at $\alpha_F \cong 30$ deg.

The drag coefficient for the body and free wing is very little changed from that for the body only for either the panel method or the experiment. The delta between the experiment and the panel method starts at about 0.1 at 0 deg and increases to about 0.2 at 30 deg. This is consistent with the nature of the wind-tunnel model, which had landing gear exposed and a number of significant gaps that were not sealed. The increasing difference with increasing body angle of attack would correspond with increasing regions of flow separation on the experimental model.

The moment coefficient is computed at the free-wing pivot point located at 20% of the free-wing root chord, which is chosen to ensure inherent aerodynamic stability of the free wing. The panel-method

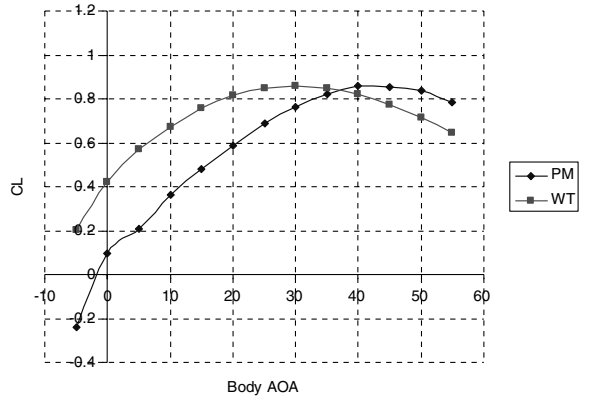

a) C_L with Boom = 0°

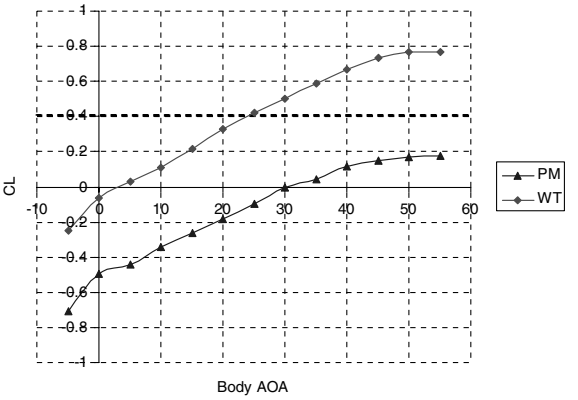

b) C_D with Boom = 50°

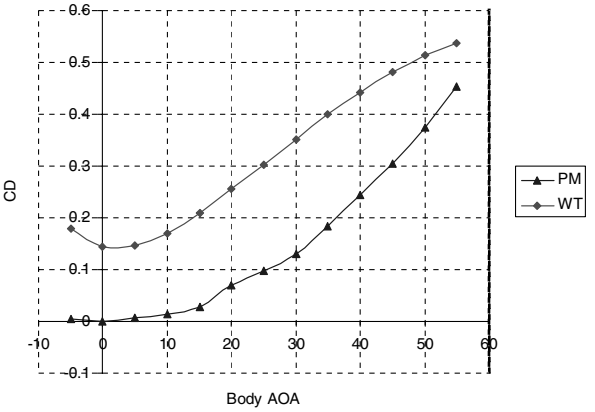

c) C_D with Boom = 0°

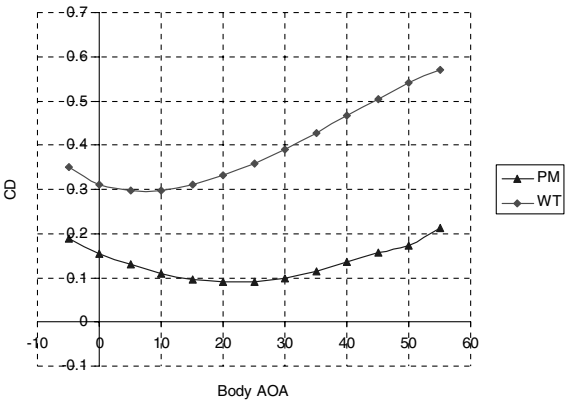

d) C_D with Boom = 50°

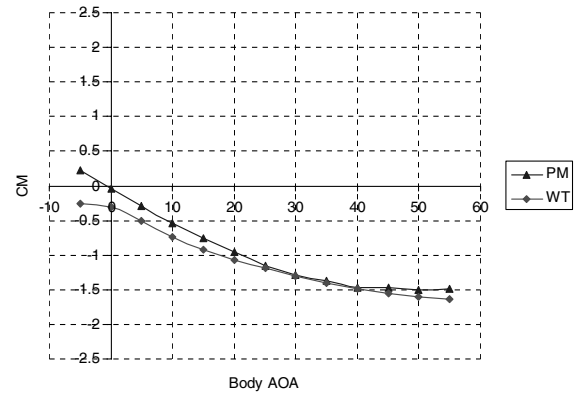

e) C_M with Boom = 0°

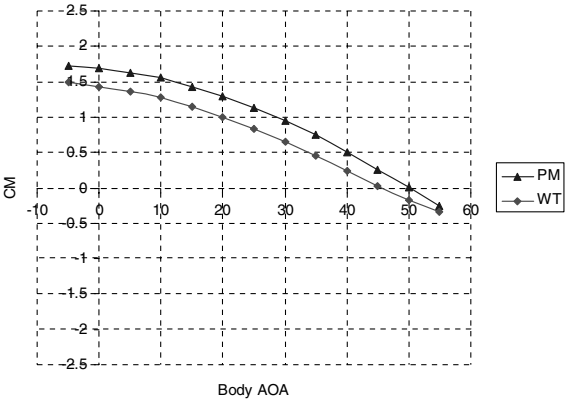

f) C_M with Boom = 50°

Fig. 14 Entire vehicle aerodynamic-coefficients comparison.

result shows a slightly positive slope with the body angle of attack, whereas the experimental curve is flat to slightly negative in slope. There is a larger difference between the body and body and free wing indicated by the experiment than indicated by the panel-method computations, as shown by Figs. 12c and 13c. These differences are small relative to the moments provided by the horizontal tail, as will be seen in the next section.

It is noted that the moment reference point is the location of the free-wing pivot, and so the difference in pitch moment between the body only and the body and free wing is due entirely to the change in aerodynamic moment on the body, due to the presence of the wing.

C. Complete Vehicle (Body, Free Wing, and Empennage)

Figure 14 shows the aerodynamic coefficients of the entire vehicle from the numerical aerodynamic analysis and from the GLMWT experimental results at two different boom angles of 0 and 50 deg.

The lift coefficients from the panel method for the complete configurations are about 0.4 less than the experimental values in the angle-of-attack range up to about 20 deg. This is similar to the difference for the body and free-wing results. The same comments apply here with respect to the possible effects of geometric differences between the panel geometry and the wind-tunnel model. The comparison of the lift curves for the 0 and 50-deg boom angles is quite interesting. For the 0-deg boom angle, the experimental and computed curves are approximately parallel for angles of attack up to a 20-deg angle of attack. The experimental curve shows a stall characteristic beginning about 20 deg, which happens for the computed curve only near 40 deg α. For the 50-deg boom-angle case, both the experimental and computed curves shift downward by a delta lift coefficient in the range of -0.5 to -0.7 and there is little indication of a stall characteristic all the way out to a body angle of attack of 45 deg. This behavior is surprising and the details of cause and effect would be very useful. These results show why it is very useful to have computed results of this type in advance of a wind-tunnel experiment. If these computed results had been available at the time the wind-tunnel experiments were conducted, then it is almost certain that explorations would have been undertaken to determine the details of the flow as needed to understand the causes.

The drag-coefficient plots (Figs. 14c and 14d) are consistent with expectations. The panel-code results show minimum induced drag, roughly corresponding to an angle of attack near zero computed lift. The experimental data indicate that the body-free wing is the source of the largest part of the drag and this leads the minimum drag point to be near the angle of attack for which this subsystem has the least drag.

The moment-coefficient curves (Figs. 14e and 14f), when compared with the moment curves for the body and the body and free wing, show that the tail dominates the pitching-moment characteristic, as expected. The computed curves are reasonably close to the experimental curves throughout the angle-of-attack range. The differences would be unacceptable for conventional vehicles with a very narrow range of operational angles of attack, but these results seem quite useful for a vehicle that is capable of operating with a body angle of attack of at least up to 50 deg.

V. Conclusions

Compared with a conventional fixed-wing aircraft, the free-wing tilt-body has far more complex aerodynamic characteristics as it undergoes large configuration changes during flight. Although the prototype has flown successfully and demonstrated ESTOL capabilities, there are many unknowns that need to be explored to be able to carry out design refinements and parameter optimization. The numerical aerodynamic analysis used in this study demonstrated effectiveness for preliminary aerodynamic analysis of this type of vehicle, as has been found in previous work on more conventional configurations.

The wind-tunnel experimental measurements reported were obtained using a model with a wing span that was about 55% of the wind-tunnel-section width. This corresponds to quite small wall corrections. Tare and interference corrections were done using analytical estimates rather than direct experimental evaluations. The net result is that the experimental measurements are believed to be within 2% of free-air values for the actual model geometry. The numerical simulation results are based on a potential flow solver with an assumed separation pattern to model the actual viscous flow. The details of the actual geometry of the experimental model and the simulation geometry are somewhat different, but generally as similar as could be achieved with available information. Therefore, the differences between the experimental results and the simulation results arise from geometric differences and from the modeling of the viscous flow using a potential flow solver with assumed separation locations. For these reasons, a direct comparison between the numerical aerodynamic analysis and the GLMWT experimental results was not feasible, but comparisons are nevertheless useful. It is believed that much closer correlation would result if the geometry of the computed and tested cases could have been made identical. Furthermore, due to the vortex-dominated flowfield, the complex wake interactions, and the presence of large separated boundary layers (especially at high body angles of attack), the numerical results would have been much more accurate if Navier–Stokes analysis had been carried out. However, carrying out such analysis for the free-wing tilt-body design would be quite laborious and expensive, because of large in-flight geometric variations. On the other hand, panel codes are relatively quick and inexpensive, yet showed ample and accurate insights for free-wing tilt-body design that are adequate enough for possible design refinements and vehicle-performance-parameter optimization studies.

There is a large scope for additional work on this type of aircraft. This paper has not addressed power effects. Interaction of the propulsion system and the airframe is an essential feature of this type of aircraft and will play a large role in determining performance and influencing stability and control characteristics.

Acknowledgments

This research is supported in part by the Michigan Space Grant Consortium (MSGC) Seed Grant and the Faculty Research and Creative Activities Support Fund (FRACASF) at Western Michigan University. The first author expresses special gratitude to Peter Garrison at AeroLogic, Inc. for his numerous suggestions in generating the panel models.

References

[1] Zuck, D. R., U.S. Patent No. 2,347,230, Apr. 1949.
[2] Spratt, C. G., U.S. Patent No. 2,623,712, Dec. 1952.
[3] Porter, R. F., Luce, R. G., and Brown, J. H., "Evaluation of the Gust Alleviation Characteristics and Handling Qualities of a Free-Wing Aircraft," NASA CR-1523, 1970.
[4] Porter, R. F., Luce, R. G., and Brown, J. H., "Investigation of the Application of the Free-Wing Principle to Light General Aviation Aircraft," NASA CR-2046, 1972.
[5] Porter, R. F., Hall, D. W., and Vergara, R. D., "Analytical Study of Free-Wing Free-Trimmer Concept," NASA CR-2946, 1978.
[6] Schmittle, H. J., U.S. Patent No. 4,596,368, June 1986.
[7] Chen, W., and Barlow, J. B., "A Wind Tunnel Test of a Tilt-Body Free-Wing Aircraft Including Thrust Effects," AIAA Paper 95-1902, June 1995.
[8] "Digital Wind Tunnel CMARC—Users' Manual," AeroLogic Inc., Los Angeles, CA, 2003.
[9] Figat, M., Goetzendorf-Grabowski, T., and Goraj, Z., "Aerodynamic Calculation of Unmanned Aircraft," *Aircraft Engineering and Aerospace Technology*, Vol. 77, No. 6, 2005, pp. 467–474.